Article

High-entropy RuO$_2$ catalyst with dual-site oxide path for durable acidic oxygen evolution reaction

Fangren Qian[1,2,3], Dengfeng Cao [1], Shuangming Chen [1]✉, Yalong Yuan[4], Kai Chen[4], Peter Joseph Chimtali[1], Hengjie Liu [1], Wei Jiang[1], Beibei Sheng[1], Luocai Yi[2,3], Jiabao Huang[2,3], Chengsi Hu[2], Huxu Lei[2,3], Xiaojun Wu [5], Zhenhai Wen [4], Qingjun Chen [2,3]✉ & Li Song [1,6]✉

Developing durable acidic oxygen evolution reaction catalysts is critical for industrial proton exchange membrane water electrolyzers. We incorporate high-entropy atoms (Co, Ni, Cu, Mn, Sm) into RuO$_2$ (RuO$_2$-HEAE) via annealing, achieving remarkably high stability (>1500 h at 100 mA cm^{-2}). In situ differential electrochemical mass spectrometry and *operando* Attenuated Total Reflection Surface-Enhanced Infrared Absorption Spectroscopy reveal RuO$_2$-HEAE follows a dual-site oxide path mechanism instead of the conventional adsorbate evolution mechanism. Quantitative Fourier-transformed extended X-ray absorption fine structure fitting and density functional theory calculations show this mechanistic shift stems from an elongated Ru-M distance in second coordination shell of RuO$_2$-HEAE, enabling direct O-O coupling. This OPM-type catalyst delivers ~1500 h of stable operation at 1 A cm^{-2} and 50 °C, demonstrating superior durability versus most reported RuO$_2$-based catalysts. This work provides fundamental insights for designing highly stable proton exchange membrane water electrolysis.

Proton exchange membrane water electrolyzers (PEMWE) are practically promising for green hydrogen generation owing to the high current density, energy efficiency, and safety[1–4]. Nevertheless, high cost and limited availability of iridium (Ir) hinder their widespread application[5–7]. Accordingly, developing high-performance and Ir-free oxygen evolution reaction (OER) electrocatalysts are crucial for progress of PEMWE[8–11]. Ruthenium dioxide (RuO$_2$) has been recognized as a replacement for IrO$_2$ in acidic OER, typically exhibiting higher activity than other oxide-based catalysts[12–14]. However, owing to the polarizing conditions of the OER, Ru atoms can be overoxidized, leading to the

formation of water-soluble RuO$_4^{2-}$ species, which compromises the stability of the electrocatalyst and results in performance degradation[15,16]. This limitation impedes the use of RuO$_2$ as an OER electrocatalyst in commercial PEM electrolyzers[17,18]. There is a need for enhanced Ru-based electrocatalysts for acidic OER. However, the quest for electrocatalysts that combine high activity and stability has remained elusive, posing an ongoing challenge for the international research community[19,20].

Over the past few decades, extensive mechanistic investigations have been conducted to understand the high initial activity of RuO$_2$ in

[1]National Synchrotron Radiation Laboratory, State Key Laboratory of Precision and Intelligent Chemistry, School of Nuclear Science and Technology, University of Science and Technology of China, Hefei, Anhui, China. [2]Key Laboratory of Rare Earths, Ganjiang Innovation Academy, Chinese Academy of Sciences, Ganzhou, China. [3]School of Rare Earths, University of Science and Technology of China, Hefei, P. R. China. [4]State Key Laboratory of Structural Chemistry, Fujian Institute of Research on the Structure of Matter, Chinese Academy of Sciences, Fuzhou, China. [5]Hefei National Laboratory for Physical Science at the Microscale, Collaborative Innovation of Center of Chemistry for Energy Materials (iChEM), School of Chemistry and Materials Sciences, University of Science and Technology of China, Hefei, China. [6]Zhejiang Institute of Photonelectronics, Jinhua, Zhejiang, China. ✉e-mail: csmp@ustc.edu.cn; qjchen@gia.cas.cn; song2012@ustc.edu.cn

the OER[21–24]. Typically, the RuO_2 follows an adsorbate evolution mechanism (AEM, Supplementary Fig. 1a), which exhibits a linear scaling relationship with a theoretical overpotential of around 0.37 V (10 mA cm^{-2})[25–27]. Consequently, considerable effort has been directed towards initiating the lattice-oxygen-mediated mechanism (LOM), which avoids the formation of $^*OOH$ intermediates and surpasses this activity threshold. Regrettably, the participation of lattice oxygen in the LOM pathway (Supplementary Fig. 1b) result in structural destabilization[28,29]. Therefore, advanced OER catalysts that function through alternative mechanisms must be discovered to tackle this existing trade-off between activity and stability[27].

Recently, a new oxide path mechanism (OPM), illustrated in Supplementary Fig. 1c, d has been suggested for OER, presenting a potentially fruitful avenue for the developing enhanced OER electrocatalysts[24,30,31]. The distinct structural arrangements of active sites, comprising pairs of metal atoms with closely spaced metal-metal distances, enable the OPM to facilitate direct coupling of O* species (O*–O*) without utilizing lattice oxygen and prevent the formation of $^*OOH$ and O vacancies[32]. Theoretically, an electrocatalyst meeting the criteria of OPM-type OER could potentially surpass the traditional scaling limit without compromising stability. Nonetheless, the durability of majority OPM-type catalysts documented in literature is restricted to low current density. Moreover, these catalysts have not been integrated with PEMWE systems, hindering their widespread practical implementation[24,30,31]. Therefore, it is crucial to create innovative OPM-type catalysts capable of withstanding high current density like 1 A cm^{-2} and promoting their application in industrial PEM reactor setups.

Drawing inspiration from the effects of multiple metal sites and high entropy effects, we have integrated high entropy atoms (Co, Ni, Cu, Mn, Sm) in RuO_2 lattice (RuO_2-HEAE). This incorporation markedly enhances the stability of the RuO_2 lattice in acidic electrolyte[33]. Notably, the RuO_2-HEAE catalyst exhibits outstanding stability, operating continuously for 1500 h without noticeable degradation at 100 mA cm^{-2}, surpassing the inferior OER stability of commercial RuO_2 (<40 h@10 mA cm^{-2}). Particularly noteworthy is the stable performance of the RuO_2-HEAE catalyst in a water electrolysis when combined with a commercial Pt/C catalyst in a practical PEM electrolyzer, sustaining operation for around 1500 h at high current density of 1 A cm^{-2}, validating its suitability for practical hydrogen generation applications. DFT calculation, *operando* Differential Electrochemical Mass Spectrometry (DEMS), and in-situ Attenuated Total Reflection Surface-Enhanced Infrared Absorption Spectroscopy (ATR-SEIRAS) have unveiled the OPM path for RuO_2-HEAE and AEM path for pristine RuO_2 catalysts, respectively. These investigations showcase how the high entropy atomic environment in RuO_2 enhances the durability of Ru and oxygen, thereby improving the durability of the OER process. Additionally, the RuO_2-HEAE catalyst exhibits heightened activity, demanding a mere overpotential of 201 mV@10 mA cm^{-2} and a cell voltage of 1.60 V to deliver high current density of 1 A cm^{-2} in PEMWE systems.

Results
Preparation and characterization of materials
An annealing method has been proposed to introduce high entropy atoms environment into the RuO_2 for RuO_2-CoNiCuMn (RuO_2-TM) and RuO_2-CoNiCuMnSm (RuO_2-HEAE) catalysts preparation (Fig. 1a–c). We incorporate chemically active 3d transition metals, including cobalt (Co), nickel (Ni), copper (Cu), manganese (Mn), and 4f rare-earth metal samarium (Sm) into the RuO_2 to enhance activity and stability[2,6]. Initially, a wet impregnation method using metal precursors was employed on a carbon black support, followed by H_2/Ar annealing reduction to produce Ru_3HEAE/C (Ru/C and Ru_3TM/C were also prepared by same method, TM: Co, Ni, Cu, Mn) nanoparticles on carbon black (Supplementary Figs. 2–5). The presence of the carbon support is

crucial in preventing particle aggregation during this process[34]. Subsequently, the Ru_3HEAE/C (Ru/C and Ru_3TM/C) material was annealed in air to transform Ru_3HEAE (Ru and Ru_3TM) nanoparticles into Ru_3HEAEO_x (RuO_x and Ru_3TMO_x) and simultaneously eliminate the carbon support (Supplementary Figs. 6–9). Lastly, the resulting Ru_3HEAEO_x (RuO_x and Ru_3TMO_x) underwent an acid-leaching step to eliminate unstable oxide species, resulting in the final catalyst known as RuO_2-HEAE (as prepared RuO_2 and RuO_2-TM).

Transmission electron microscopy (TEM) images (Supplementary Fig. 10) clearly demonstrated that RuO_2-HEAE catalysts were uniform in size (~4.4 nm, Fig. 1d). High-angle annular dark-field scanning TEM (HAADF-STEM) patterns showed high crystallinity in the RuO_2-HEAE nanoparticles, having distinct lattices (Fig. 1e, f), and these fringes can be attributed to the (101) and (200) planes of RuO_2 (Fig. 1f). The X-ray diffraction (XRD) results of as prepared RuO_2, RuO_2-TM and RuO_2-HEAE showcased characteristic peaks of rutile RuO_2 (JCPDS #40-1290) having a dominant (110) peak at 28° (Fig. 1g)[35]. This vindicates that incorporation of high entropy atoms environment did not alter the RuO_2 lattice structure. Energy-dispersive spectroscopic elemental mapping (Fig. 1h) was used to verify these high entropy atoms and Ru were uniformly dispersed in RuO_2-HEAE without segregation. In addition, RuO_2 nanoparticles were prepared without introduction of foreign element (as prepared RuO_2) and incorporate 3d transition metals into RuO_2 (RuO_2-TM) as a control sample. The RuO_2 and RuO_2-TM materials demonstrated similar morphology compare to RuO_2-HEAE, having a particle size of about 4.5 nm (Supplementary Figs. 11 and 12). As shown in Supplementary Table 1, the introduction of transition metal elements into RuO_2 is approximately 1 at%, suggesting that only trace amounts of foreign metal elements have been introduced into the lattice, without causing a phase transition in RuO_2.

Local structure of catalysts
X-ray absorption near-edge structure (XANES) and extended x-ray absorption fine structure (EXAFS) techniques were conducted to elaborate the chemical states and the coordination environments of the as prepared materials, respectively[33]. Ru-K XANE of RuO_2, RuO_2-TM and RuO_2-HEAE locate at the similar energy as that of c-RuO_2, while positive shift compares to that of Ru foil, revealing a Ru^{4+} in RuO_2, RuO_2-TM and RuO_2-HEAE (Supplementary Fig. 13). The similarity in the adsorption edge and white peaks of RuO_2, RuO_2-TM, and RuO_2-HEAE compared to that of c-RuO_2, may be due to the analogy in the coordination structure (Fig. 2a) as revealed in EXAFS[36]. The EXAFS patterns for first coordination shell of RuO_2 is fitted by a mixture of Ru_1-O (1.90 Å) and Ru_2-O (1.99 Å) coordination paths with Ru-O coordination numbers (CN) of 2.0 (Ru_1-O) and 4.0 (Ru_2-O), respectively[37]. Moreover, the second coordination shell of Ru-metal for RuO_2 are also fitted by a mixture of Ru-M_1 (3.11 Å) and Ru-M_2 (3.55 Å) bond with Ru-M coordination numbers of 2.0 (Ru-M_1) and 8.0 (Ru-M_2), respectively (Supplementary Fig. 14 and Supplementary Table 2). Then, the first coordination shell of RuO_2-TM is also fitted by a mixture Ru_1-O and Ru_2-O path and the bond length increases to 1.86 and 1.98 Å, respectively and the CN is 1.7 and 4.2, respectively. The second coordination shells of Ru-metal for RuO_2-TM are fitted by a mixture of Ru-M_1 (3.10 Å) and Ru-M_2 (3.54 Å) bond with Ru-M coordination numbers of 1.9 (Ru-M_1) and 6.7 (Ru-M_2), respectively (Supplementary Fig. 15 and Supplementary Table 3). As shown in Fig. 2b and Supplementary Table 4, the first coordination shell of RuO_2-HEAE is also fitted by a mixture of Ru_1-O and Ru_2-O path and the bond length returns to 1.86 and 1.98 Å, respectively and the CN is 1.8 and 4.2. The second coordination shell of Ru-metal for RuO_2-HEAE is fitted by a mixture of Ru-M_1 (3.11 Å) and Ru-M_2 (3.54 Å) bond with Ru-M coordination numbers of 2.0 (Ru-M_1) and 6.7 (Ru-M_2), respectively. According to Fig. 2c, the bond length of Ru-M_1 in RuO_2 lattice is controlled by the high entropy atomic environment, which further controls the reaction species anchored on metal sites. The oxidation states in RuO_2-HEAE can be obtained from the TM (TM: Co, Ni, Cu, Mn) K-edge
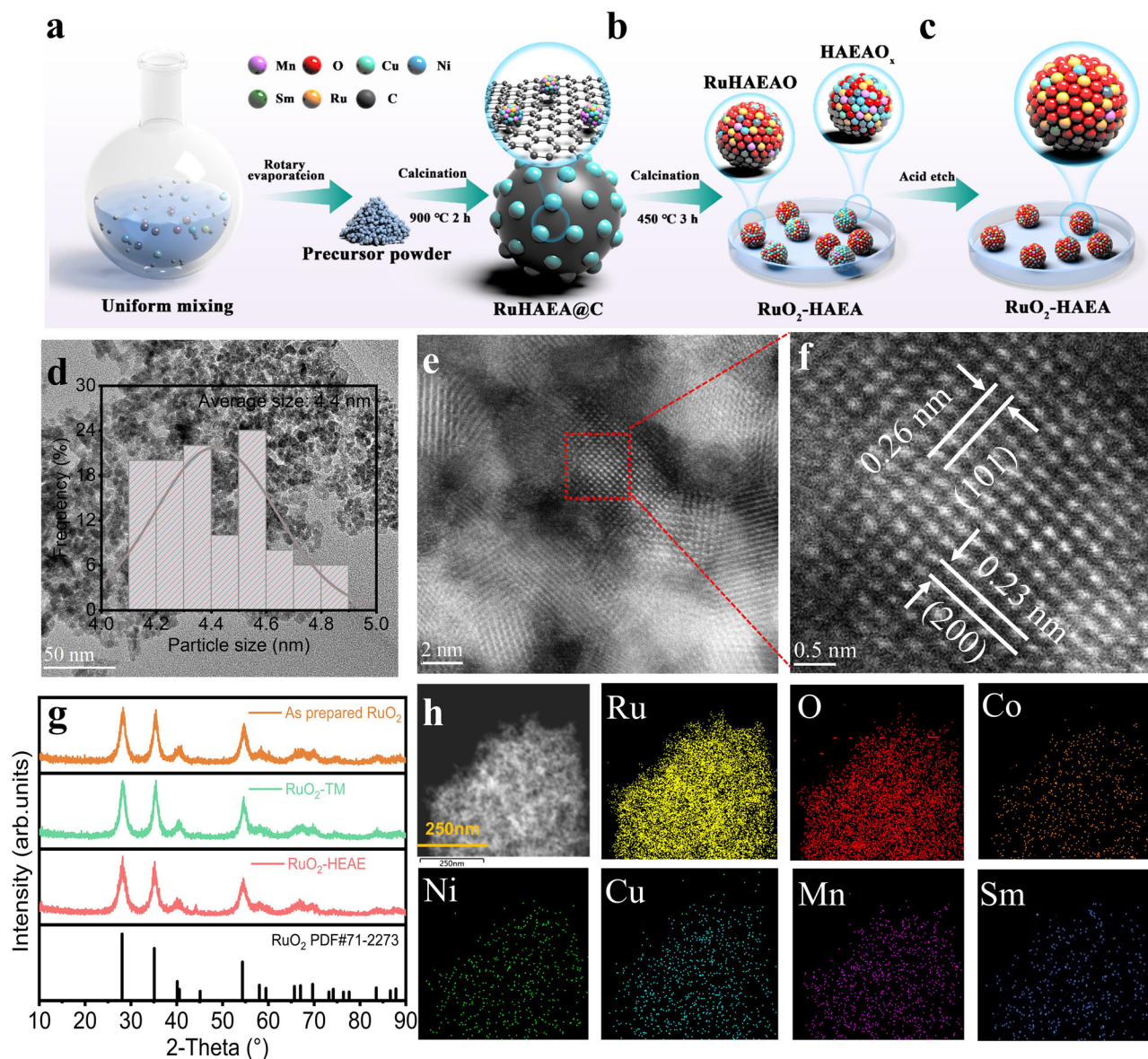
Fig. 1 | Preparation and characterization of RuO$_2$ based materials. a–c Schematic illustrating the synthesis of RuO$_2$ based catalysts. **d** The size distribution of RuO$_2$-HEAE. **e** High-angle annular dark-field STEM images of RuO$_2$-HEAE. **f** Magnified HAADF-STEM image of RuO$_2$-HEAE. **g** X-ray diffraction results of RuO$_2$ based materials. **h** elemental mappings of the RuO$_2$-HEAE.

XANES (Supplementary Figs. 16–18). The EXAFS spectrum of RuO$_2$-HEAE at the TM K-edge showed a main peak at around 2 Å (Fig. 2d–f and Supplementary Fig. 19), assigned to the TM-O coordination and the second shell attributed to TM-M$_1$ and TM-M$_2$, which are consistent with the results of Ru, confirming the high entropy atoms environment in RuO$_2$ not the oxides. Supplementary Figs. 20 and 21 and Supplementary Table 5 show that the coordination number and bond length of Co-O in RuO$_2$-HEAE is 4.4 and 1.9 Å, respectively. Similar results are obtained for the other metals as shown in Supplementary Figs. 22–25 and Supplementary Tables 6 and 7) clearly vindicating homogenous distribution of TM in the RuO$_2$ structure. The k^3-weighted WT EXAFS spectra for RuO$_2$-HEAE showed a similar contour profile in k-space to that of RuO$_2$ with the contour intensity maximum shift from 12.9 Å^{-1} to 13.3 Å^{-1} (Fig. 2g–i). These findings confirm that the local structure in RuO$_2$ lattice is controlled by the high entropy atomic environment.

Electrochemical OER and PEMWE performance

The OER performance of as prepared materials was assessed in 0.1 M HClO$_4$ solution by employing a standard three-electrode system. As

prepared RuO$_2$, RuO$_2$-TM, and commercial RuO$_2$ nanoparticles (c-RuO$_2$) were used as control samples. According to the results of linear sweep voltammetry (LSV), the obtained RuO$_2$ demonstrated superior OER activity than c-RuO$_2$, attributed to the small size (Fig. 3a). Representative LSV curves without iR compensation (Supplementary Fig. 26a). The overpotential for c-RuO$_2$ is 325 mV@10 mA cm^{-238}. Integration of transition metals (Co, Ni, Cu, Mn) boosted the OER activity of RuO$_2$ (214 mV@10 mA cm^{-2}). Interestingly, the integration of rare earth (Sm) and transition metals (Co, Ni, Cu, Mn) into RuO$_2$ (RuO$_2$-HEAE, 201 mV@10 mA cm^{-2}) further boosted OER activity and the overpotential at the higher current densities was quickly decreased due to the smaller Tafel slope of RuO$_2$-HEAE (33.31 mV dec^{-1}) compared with both RuO$_2$-TM (51.67 mV dec^{-1}), as prepared RuO$_2$ (83.81 mV dec^{-1}) and c-RuO$_2$ (162.75 mV dec^{-1}) (Fig. 3d). Electrochemical impedance spectroscopy (EIS) (Supplementary Fig. 27) shows a small R_{ct} (29.6 Ω) for RuO$_2$-HEAE compared to RuO$_2$-TM (53.7 Ω), as-prepared RuO$_2$ (53.4 Ω), and c-RuO$_2$ (75.0 Ω), showing a superior charge transfer and improved OER kinetics. The electrochemically active surface areas (ECSA) of various catalysts were
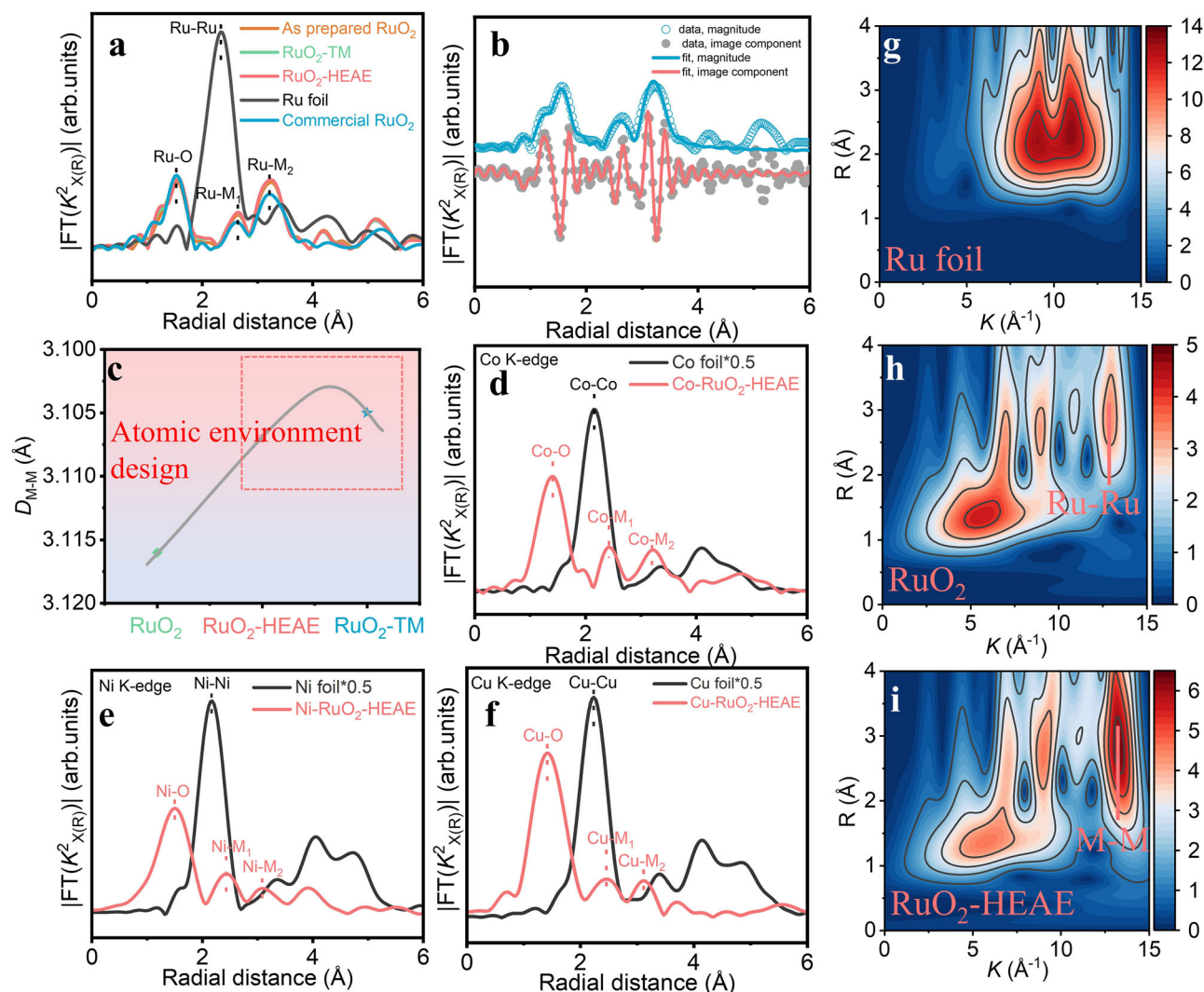
Fig. 2 | Local structure of RuO$_2$ based catalysts. a R-space EXAFS spectra at Ru K-edge of as prepared RuO$_2$, RuO$_2$-TM, RuO$_2$-HEAE, C-RuO$_2$, and Ru foil. **b** FT-EXAFS fitting of Ru for the RuO$_2$-HEAE at R space. **c** the distance between bimetallic sites was regulated by atomic environment design. **d–f** R-space EXAFS spectra at Co, Ni, and Cu K-edge of the RuO$_2$-HEAE., k^3-weighted WT-EXAFS contour plot for (**g–i**), Ru foil, RuO$_2$, and RuO$_2$-HEAE, respectively.

calculated by determining the double-layer capacitance (C_{dl}) from the cyclic voltammogram (CV) curves in the non-Faradaic region (Supplementary Fig. 28). The C_{dl} (Supplementary Fig. 29) for RuO$_2$-HEAE was calculated to be 3.95 mF cm^{-2}, larger than RuO$_2$-TM (5.74 mF cm^{-2}), as prepared RuO$_2$ (4.75 mF cm^{-2}), and c-RuO$_2$ (3.40 mF cm^{-2}). Remarkably, both EIS and kinetic assessments concur with the LSV results. The calculations of turnover frequency (TOF) of catalysts show that the RuO$_2$-HEAE yields a turnover TOF of 871.83 h^{-1}, which is 8.0, 58.88, and 347.34 times greater than that of RuO$_2$-TM as prepared RuO$_2$ and c-RuO$_2$, respectively (Fig. 3b). Moreover, we conducted electrochemical performance tests on catalysts synthesized from different batches. The error analysis between different batches of RuO$_2$-based catalysts revealed a high degree of similarity in performance among catalysts from different batches (Supplementary Fig. 30a–c), confirming the reliability and reproducibility of the electrochemical performance data and the specific activities of RuO$_2$-HEAE normalized by the ECSA were markedly greater than those of RuO$_2$-TM as prepared RuO$_2$ and c-RuO$_2$ (Supplementary Fig. 30d). In general, the RuO$_2$-HEAE catalyst demonstrates the highest intrinsic activity, potentially attributed to a distinct OER mechanism. Electrochemical stability is another important factor in electrocatalyst design for commercial application in proton exchange membrane electrolyzers. Long-term stability for

OER of RuO$_2$-HEAE was analyzed by chronopotentiometry (CP) technique at 100 mA cm^{-2}. As shown in Fig. 3c, RuO$_2$-HEAE showed stability for 1500 h with the current density of 100 mA cm^{-2}. Dissolution kinetics analyses were performed on the dissolved metal elements during the reaction, which are influenced by operational parameters such as the applied overpotential and the concentration of cations in the solution. The dissolution rate of Ru in RuO$_2$-HEAE remains consistently low throughout the entire stability testing process, with its dissolution being nearly negligible. Compared to Ru, the other introduced non-noble metals exhibit relatively higher dissolution rates, yet even after 1500 h of reaction at a high current density of 100 mA cm^{-2}, the dissolution rates of all non-noble metals remain below 40% (Supplementary Fig. 31). The results show that the incorporation of a high entropy atomic environment in RuO$_2$ guarantees the stability of the active site, thereby enhancing corrosion resistance. In summary, the RuO$_2$-HEAE indicated outstanding OER performance compared to RuO$_2$-based acidic OER materials recently reported (Supplementary Fig. 26b and Supplementary Table 8). An PEM electrolyzer system (Fig. 3e) with the RuO$_2$-HEAE (or c-RuO$_2$) as an anode and Pt/C as a cathode was employed to assess practical application under simulated industrial conditions. The current-voltage (I-V) in Fig. 3f give RuO$_2$-HEAE shows better performance compared to commercial RuO$_2$
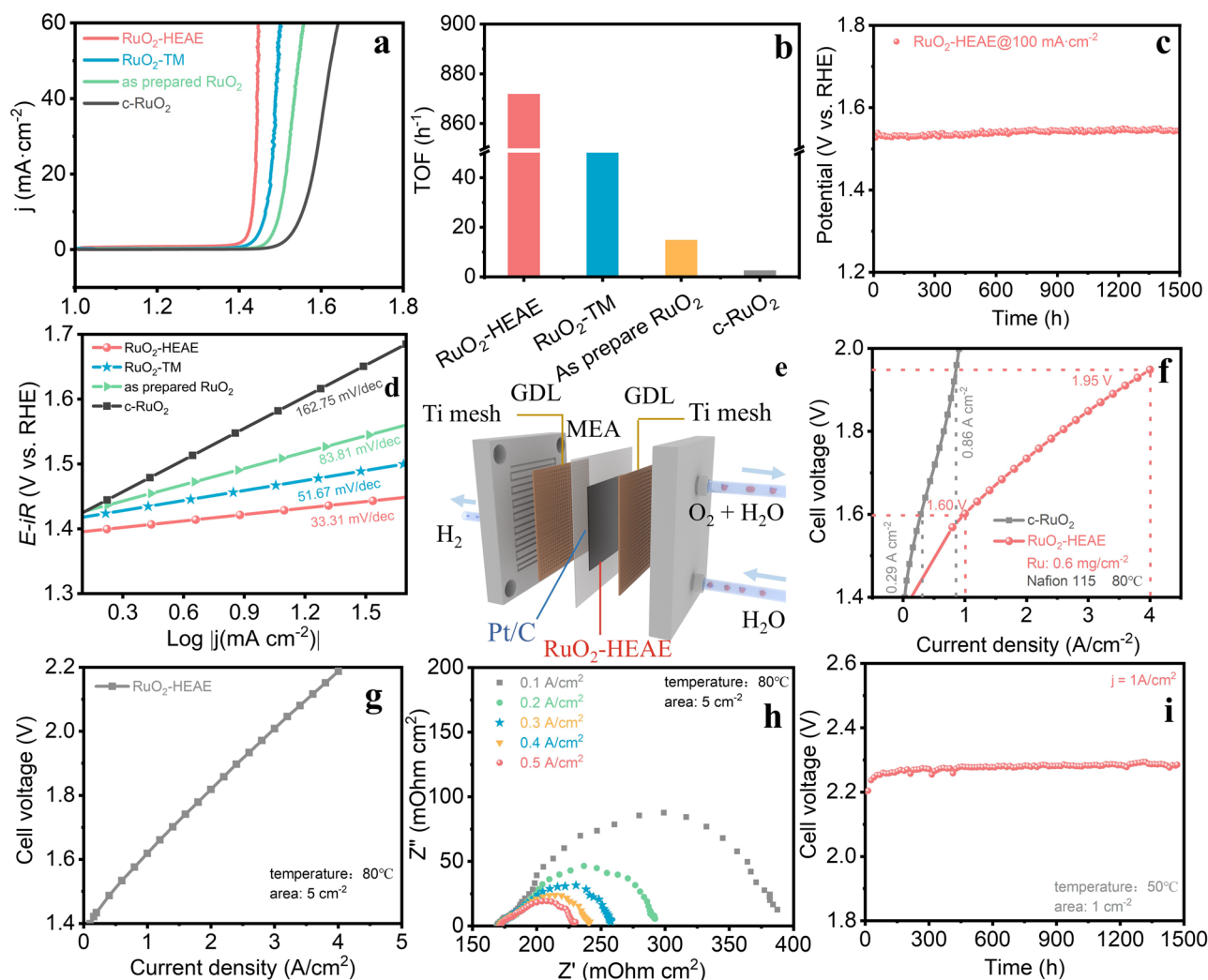
Fig. 3 | Performance investigations. a Representative LSV for RuO$_2$-HEAE, RuO$_2$-TM, as prepared RuO$_2$ and commercial RuO$_2$ in 0.1 M HClO$_4$ at a scan rate of 5 mV s^{-1} **b** Comparison of apparent TOF of RuO$_2$-HEAE, RuO$_2$-TM, as prepared RuO$_2$ and commercial RuO$_2$. **c** Chronopotentiometric curve of RuO$_2$-HEAE during the OER at 100 mA cm^{-2}, showing the enhanced stability of the electrocatalyst in comparison with com. RuO$_2$. The voltages were not IR compensated.

d Corresponding Tafel slopes derived from LSV for RuO$_2$-based catalysts. **e** Schematic of the PEMWE device. **f** I-V curves of PEMWEs the RuO$_2$-HEAE and commercial RuO$_2$ catalysts as anodes, commercial Pt/C as cathode. **g** I-V curves of PEMWEs the RuO$_2$-HEAE at 80 °C (area: 5 cm^2). **h** Operando EIS measurements of PEMWE. **i** Durability of RuO$_2$-HEAE at 1 A cm^{-2} in the PEMWEs.

(0.29 A cm^{-2}), achieving high current density of 1 A cm^{-2} at 1.6 V. With an increase in temperature, the current density of PEMWE sharply rises at the same cell voltage (Supplementary Fig. 32). To further validate the practicality of the RuO$_2$-HEAE catalyst in actual PEMWE applications, we assembled a larger electrolyzer cell (5 cm^2). The results indicate that a 5 cm^2 electrolyzer cell exhibited a current density of 1 A cm^2 at a cell voltage of 1.62 V (Fig. 3g). Remarkably, the water electrolysis performance of the electrolyzers remains consistent even with an increase in electrode area from 1 cm^2 to 5 cm^2. To further elucidate the significantly enhanced performance of RuO$_2$-HEAE catalysts in PEMWE, EIS Nyquist plots of the electrolyzer reveal three distinct resistances: ohmic resistance (OR), charge-transfer resistance (CTR), and mass transport resistance (MTR) (Fig. 3h). The high-frequency intercept corresponds to OR, while the arcs in high- and low-frequency regions represent CTR linked to electrochemical reactions and MTR associated with reactant/product transport, respectively. The OR values of RuO$_2$-HEAE are nearly identical, with low CTR and MTR, indicating superior activity due to enhanced charge transport and reduced mass transfer resistance. Figure 3h demonstrates the application of operando EIS at different currents to evaluate the charge

transfer resistance of RuO$_2$-HEAE. The results indicate a significant decrease in resistance with increasing current, implying improved electron transfer rates and enhanced energy conversion efficiency at higher currents during electrolysis. Additionally, the stability of the RuO$_2$-HEAE catalyst was assessed under conditions of 50 °C and a high current density of 1 A·cm^{-2}. As shown in Fig. 3i, the catalyst exhibited notable stability over a 1500 h electrolysis period, with an activity degradation rate of only 0.05 mV h^{-1}, further affirming its potential for practical application.

Insights into the catalytic mechanism

We conducted the *operando* XAFS experiments to gain deeper insights into the dynamic evolution of the electronic and coordination structure of the Ru during the OER process[11,39,40]. The in-situ XAFS testing environment of RuO$_2$ as shown in Supplementary Fig. 33 and the adsorption edge of Ru is located at the similar energy both ex-situ and open-circuit voltage (OCV), according to the results of Ru K-edge XANES (Fig. 4a). After applying voltage, the near edge of Ru shifts to the higher energy, an indication of increased average oxidation state of Ru during the electrocatalytic OER. This emanates from the transfer of
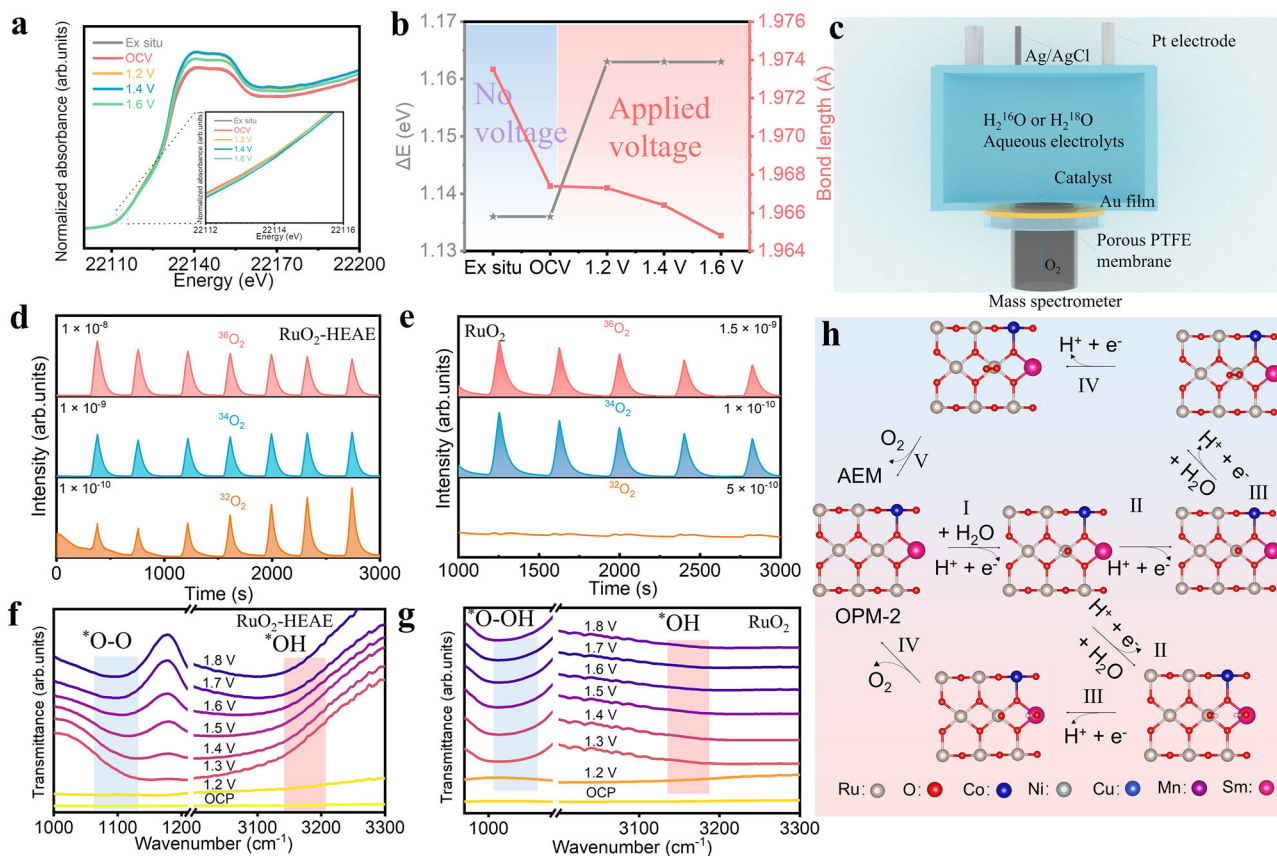
Fig. 4 | Mechanism investigations of the enhanced OER activity of RuO₂-HEAE.
a *Operando* XANES of RuO₂-HEAE during the OER process. **b** Relationship between normalized absorption edge energy during the OER process. **c** Schematic illustration of the *in-suit* DEMS. **d**, **e** DEMS signals of $^{32}O_2$ [$^{16}O^{16}O$, mass/charge ratio (m/z) = 32], $^{34}O_2$ ($^{16}O^{18}O$, m/z = 34), and $^{36}O_2$ ($^{18}O^{18}O$, m/z = 36) from the gaseous products for ^{18}O-labeled RuO₂ (**e**) and RuO₂-HEAE (**f**) catalysts in $H_2^{18}O$ aqueous HClO₄ electrolyte. **f**, **g** In-suit ATR-SEIRAS for (**g**) RuO₂ and (**h**) RuO₂-HEAE. **h** Proposed OER mechanism for as-prepared RuO₂-HEAE and RuO₂, based on the Operando DEMS and ATR-IR measurements.

electrons from Ru to nearby adsorbed oxygen species, thus enhancing rapid oxidation reaction[11]. The local structure and coordination environment are tracked by EXAFS analysis. The EXAFS and FT-EXAFS fitting spectra of the Ru K-edge (Supplementary Figs. 34 and 35 and Supplementary Table 9) reveal a dominant peak at ~2 Å, which is attributed to the first shell of the Ru-O. With regards to the ex-situ state, the first-shell peak intensified at an applied potential and showed a slight negative shift. These findings signify reconstruction of the local atomic environment of Ru sites during the OER, as a result of the adsorbed oxygen species over Ru sites[41]. According to Fig. 4b, an obvious positively related between the absorption edge location and the applied voltage is evidenced. With increasing voltage, the oxidation state of Ru slightly increases, whereas the Ru-O bond length slightly shortens (Fig. 4b), shows an increase in bonding energy to resist the dissolution of the Ru-O bond.

We employed a combination of various characterization techniques to assess the structural stability of the examined catalysts. The surface morphology and crystal structure of the RuO₂-HEAE catalyst post-OER remained unchanged (Supplementary Figs. 36 and 37a). Subsequent high-resolution Ru XPS spectra revealed that the Ru 3p binding energies for RuO₂-HEAE post-OER tests displayed only a positive shift of 0.2 eV, respectively, compared to their pre-reaction states (Supplementary Fig. 37b), suggesting that the high entropy atomic environment protect the RuO₂-HEAE catalyst to prevent over-oxidation of Ru sites. As shown in Supplementary Fig. 38, we utilized DFT calculations to further theoretically elucidate the stability mechanism of RuO₂-HEAE. The Bader charge analysis reveals obvious electron transfers, leading to an increase in the charge of Ru

progressively from 1.74 (RuO₂) to 1.90 (RuO₂-TM), 2.08 (RuO₂-HEAE) (Supplementary Fig. 38a). This observation confirms the introduction of a high entropy atomic environment leads to a redistribution of charges around Ru. To assess the stability of Ru and lattice oxygen, we computed the formation energy of Ru vacancy (ΔG_{Ru} vacancy) and lattice oxygen (ΔG_O vacancy) and, which are used in tandem to evaluate the stability of the electrocatalysts. RuO₂-HEAE demonstrates the highest ΔG_{Ru} vacancy at 6.87 eV, surpassing RuO₂, and RuO₂-TM by 3.58 and 5.89 eV, respectively (Supplementary Fig. 38b). Particularly, the modulation of Ru-O covalency results in a modified ΔG_O vacancy, increasing from 3.00 eV in RuO₂ to 3.27 and 3.75 eV for RuO₂-TM and RuO₂-HEAE, respectively (Supplementary Fig. 38c). When considering both ΔG_{Ru} vacancy and ΔG_O vacancy together, the stability of RuO₂-based catalysts follows an increasing trend based on Ru-O covalency. This validates the proposed design principle that enhanced the durability of RuO₂ by integrating high entropy atomic environment.

Isotope-labeled operando DEMS measurements were conducted in 0.1 M HClO₄ $H_2^{18}O$ and $H_2^{16}O$ electrolytes (Supplementary Fig. 39 and Fig. 4c–e) to understand the OER mechanism occurring on RuO₂-HEAE and RuO₂[42,43]. First, RuO₂ and RuO₂-HEAE were labeled with ^{18}O by employing five cycles in the 0.1 M HClO₄ with ^{18}O solution. Subsequently, the ^{18}O-labeled materials were rinsed with pure water to get rid of $H_2^{18}O$, and then cycled in 0.1 M HClO₄ solution. The generation of O_2, including $^{32}O_2$ ($^{16}O^{16}O$), $^{34}O_2$ ($^{16}O^{18}O$), and $^{36}O_2$ ($^{18}O^{18}O$) were detected by DEMS. The O_2 is generated via three pathways: (i) from two water molecules ($H_2^{16}O$) without involvement of lattice oxygen ($^{16}O^{16}O$), (ii) the combination of one water molecule ($H_2^{16}O$) and a lattice oxygen (^{18}O), and (iii) only from two lattice oxygen[44,45]. As depicted

in Fig. 4d, e, RuO$_2$ produced ^{36}O$_2$ and ^{34}O$_2$, while the ^{32}O$_2$ was not generated as revealed by DEMS (Fig. 4e), while the ^{32}O$_2$ were probed on RuO$_2$-HEAE in H$_2$^{18}O electrolyte (Fig. 4d). Note that the remaining surface H$_2$^{16}O adsorbates may participate in the OER process to generate ^{32}O$_2$ products. For OPM OER, the ^{16}O$_{ads}$ on neighboring metal sites possibly couple together to form ^{32}O$_2$, while the ^{32}O$_2$ was not probed from the background via non-OPM pathway[30]. Hence, as hinted by DEMS measurements, the RuO$_2$ follow the AEM path while the RuO$_2$-HEAE follow the OPM path bypassing the *OOH species (Fig. 4h). The *OH is a common intermediate in the OPM-type OER, and the resulting *OH intermediates are electrophiles that can react with nucleophiles such as methanol. The increased *OH adsorption was experimentally confirmed using methanol as a probe (Supplementary Fig. 40). The methanol oxidation reaction (MOR) follows a known mechanism where methanol molecules tend to nucleophilically interact with the electrophilic *OH. Consequently, MOR exhibits higher activity on surfaces with stronger *OH adsorption. Upon introducing 0.1 M methanol into the 0.1 M HClO$_4$ solution, the current densities of RuO$_2$-HEAE exhibited a significant increase compared to before the methanol addition, attributed to methanol electrooxidation, while, in RuO$_2$, there was almost no significant difference in current density before and after the addition of methanol. The larger current difference observed between MOR and OER over RuO$_2$-HEAE compared to RuO$_2$ indicated a stronger MOR competition reaction, confirming the enhanced *OH adsorption on RuO$_2$-HEAE. The significant enhancement in *OH adsorption indicates that RuO$_2$-HEAE may potentially follow the OPM reaction pathway.

Operando ATR-SEIRAS (Supplementary Fig. 41) was utilized to characterize potential-dependent oxygen intermediates (*OH, *O, *OOH, or -O-O-) during the OER for RuO$_2$-HEAE and reference samples due to its vulnerability to surface reaction species[46]. In the case of commercial RuO$_2$, a distinct *OOH intermediate associated with the AEM pathway was observed at approximately 1000 cm^{-1} (Fig. 4g), indicating its significance as the rate-determining step. The incorporation of HEAE into RuO$_2$ introduced a distinct peak at 1100 cm^{-1}, attributed to the O-O stretching vibrations of -O-O- species, which result from oxygen bridging between neighboring active sites (Fig. 4g)[47,48]. These -O-O- species are recognized as crucial intermediates in the OPM-type of OER. The *OH is a classic species via OPM-type path, and its voltage-dependent peak is located at around 3100 cm^{-1} (Fig. 4f, g)[40]. In conclusion, the *in-suit* DEMS and ATR-SEIRAS successfully detected the isotope-labelled O$_2$ from the OPM-type OER and the reaction intermediates in RuO$_2$-HEAE. We propose that the high entropy atomic environment constructed in RuO$_2$ trigger dual-site OPM based on the operando measurements (Fig. 4h).

To further explore the impact of high entropy atomic environment (Co, Ni, Cu, Mn and Sm) on OER mechanism of RuO$_2$, DFT calculations were carried out by employing RuO$_2$, RuO$_2$-TM (Co, Ni, Cu and Mn), RuO$_2$-HEAE (Co, Ni, Cu, Mn and Sm). To establish a rational model, a set of 200 random models in which HEAE replaces Ru site were scanned according to energy (Supplementary Figs. 42–81). Subsequently, the model with highest durability was used for catalysis calculations. The project density of states in Fig. 5a demonstrate the metallicity of RuO$_2$ and RuO$_2$-HEAE. The metallic-like conductor featured by the O 2p and Ru 4d of RuO$_2$ dominating the Fermi level (EF) concurs with previous computational studies[49–51]. We further analyzed different OER paths (Fig. 4h and Supplementary Fig. 82) to establish the favorable OER path among AEM, LOM, and OPM (Supplementary Figs. 83–94)[52]. For clean RuO$_2$, stronger binding of *OOH adsorbates (ΔG_{OOH} = 3.56 eV) led to the AEM path: H$_2$O → *OH → *O → *OOH → O$_2$[53]. The generation of *OOH is the rate determining step (RDS) having a large activation energy of 0.97 eV, which is similar to previous work[54]. However, higher activation energy of RDS (LOM 3.58 eV and OPM 2.80 eV) were evidenced in the LOM and OPM paths (Supplementary Fig. 95). For RuO$_2$-TM, the introduction of transition metal gave a

higher activation energy of 1.37 eV for *OOH generation for AEM path. Meanwhile, a decreased activation energy of RDS (OPM 0.88 eV) for OPM path was observed (Supplementary Fig. 96). Therefore, the introduction of TM in RuO$_2$ turns the OER path from AEM into OPM. More interestingly, the introduction of high entropy atomic environment in RuO$_2$ is more favorable, having a smaller ΔG_{max} of 1.46 eV for the third step, due to the varying adsorbability of reaction species on the two sites, thus further promoting the O-O coupling, and leading to the generation of O$_2$ (Fig. 5b and Supplementary Fig. 97). The O-O coupling follows the OPM path depending on the distance between bimetallic sites. If the adjacent metal is too close, it is easy to form *OOH intermediates and follows the AEM path. The O-O coupling becomes difficult if the adjacent metal is too far. As shown in Fig. 5c, the distance between bimetallic sites in RuO$_2$ lattice from experiments and DFT calculations results are effectively modulated by introducing TM and high entropy atomic environment and consequently triggering the OPM path from AEM. The process of O-O coupling is further analyzed by CINEB method and Fig. 5d and Supplementary Figs. 98 and 99 intuitively illustrates the two adjacent adsorbed O gradually couple to complete O$_2$ evolution process. As illustrated in Fig. 5e, the energy barrier of O-O coupling is substantially decreased from 1.14 to 0.054 eV following the introduction of high entropy atomic environment in RuO$_2$ lattice. This explicitly confirms that the RuO$_2$-HEAE trigger OPM-type OER path. Further, crystal orbital Hamilton population (COHP) of Ru-O, Ru⋯Ru, and Ru⋯TM, were analyzed on the RuO$_2$ and RuO$_2$-HEAE surfaces to explore the effect of high entropy atomic environment on the structural stabilization of RuO$_2$. Figure 5f, g shows that the integrated COHP (ICOHP) value of Ru-O in RuO$_2$-HEAE is larger than in pristine RuO$_2$ (−2.08 eV versus −1.74 eV), showing an intensified Ru-O in RuO$_2$-HEAE. Additionally, a negative ICOHP value of Ru⋯Sm was revealed in the RuO$_2$-HEAE (−0.15 eV), indicating a weak long range orbital coupling between dopants and the vicinal Ru sites. On the contrary, no obvious interaction of Ru⋯Ru (0.004 eV for ICOHP) in RuO$_2$ was evidenced. Hence, the Ru sites may be further strengthened by the integration of high entropy environment. The enhanced stability owing to the integration of high entropy atomic environment in RuO$_2$ is also confirmed by the de-metallization ability of Ru and others atoms (Fig. 5h and Supplementary Figs. 100–102). The integration of high entropy atomic environment makes the Ru and lattice oxygen de-metallization become more difficulty, and thus stabilizing the RuO$_2$. The high entropy atoms, especially Sm atom possess relatively higher de-metallization energies. The energy change of the lattice oxygen loss was used to estimate the durability of lattice oxygen (Supplementary Fig. 103). The enthalpy changes for subsurface oxygen loss were calculated to be 1.74 and 2.08 eV on the pure RuO$_2$ and RuO$_2$-HEAE surface, respectively, obviously confirming that the integrated high entropy atoms to the RuO$_2$ lattice had also stabilized lattice oxygen. These finding suggest that the RuO$_2$ lattice becomes more durable after the integration of high entropy atomic environment.

Discussion

In summary, we constructed high entropy atomic environment in RuO$_2$ lattice by using a two-step calcination strategy generating RuO$_2$-HEAE, a highly active and durable a non-iridium-based acid-stable OER electrocatalyst. The catalyst demonstrated a low overpotential of 201 mV at 10 mA cm^{-2} and a low degradation for OER over 1500 h at 100 mA cm^{-2} in an acidic electrolyte. A PEMWE using RuO$_2$-HEAE catalyst can steadily operate at 1 A cm^{-2} for approximately 1500 h. Combination of extensive in-situ techniques and DFT calculations confirm the RuO$_2$-HEAE follows the OPM path during OER process, in which the direct O-O coupling is the vital process. Consequently, overpotential limitations resulting from the conventional AEM mechanism are suppressed. The introduction of high entropy atomic environment in RuO$_2$ not only triggers the OPM path but also ensures stability of active site, thus boosting corrosion resistance. By leveraging on geometric
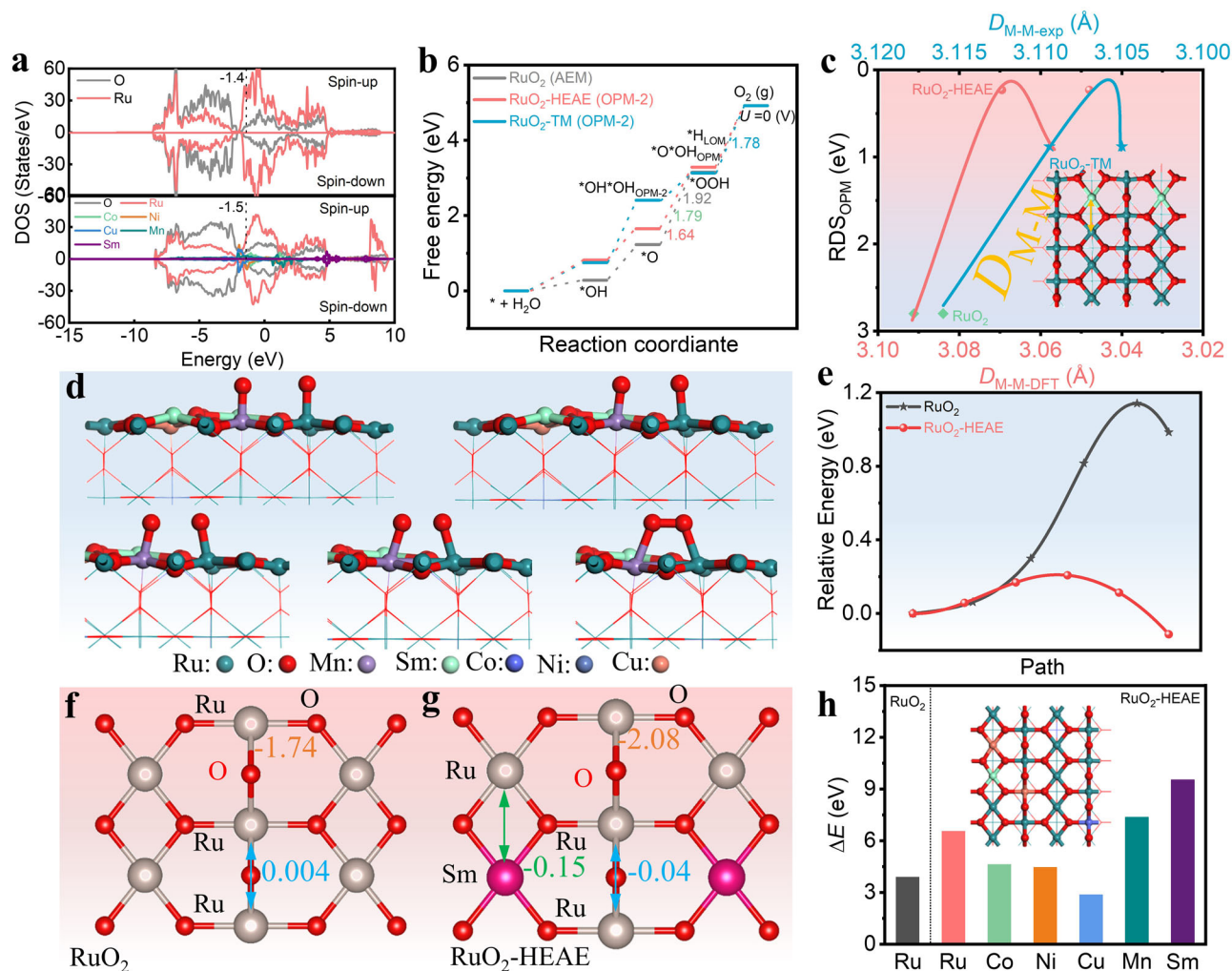
Fig. 5 | OER mechanism by DFT calculations. a PDOS of RuO_2 and RuO_2-HEAE, the dashed lines are the location of (**d**) band centers. **b** Free energy profiles of RuO_2, RuO_2-TM, and RuO_2-HEAE in OER pathways. **c** The relationship between the RDS of OPM path and the distance between bimetallic sites from both experiments and DFT calculations. **d** the schematic illustration for the process of O-O coupling on RuO_2-HEAE catalyst. **e** the energy barrier for the process of O-O coupling. **f, g** ICOHP of Ru-O, Ru⋯Ru, Ru⋯Sm on the surfaces of RuO_2, RuO_2-HEAE. **h** De-metallization energies of Ru from RuO_2, and Ru and other atoms from RuO_2-HEAE.

structural engineering of the metal active sites, our work delves into a reaction pathway that enhances OER performance.

Methods

Chemicals

$RuCl_3 \cdot xH_2O$ (99.99%), $CoCl_2 \cdot 6H_2O$ (99.99%), $NiCl_2 \cdot 6H_2O$ (99.90%), $CuCl_2 \cdot 6H_2O$ (99.99%), $MnCl_2 \cdot 4H_2O$ (99.99%), and $SmCl_3 \cdot 6H_2O$ (99.00%) were purchased from Macklin without further purification. Commercial RuO_2 (ruthenium content, 75%+) was purchased from Suzhou Sinero Technology Co., Ltd., China. ^{18}O Water (^{18}O, 97%) was purchased from Macklin. Hydrochloric acid (HCl, 36–38%, Macklin), Nafion (5 wt%, Sigma-Aldrich). Methanol (CH_3OH, 99.9%, Macklin). The carbon fiber paper (TGP-H-060) was purchased from Toray Industries Perchloric acid ($HClO_4$, 70–72%, XiLong Scientific). The water used in this work is distilled water, with a conductivity of 2.9 μS cm⁻¹ unless otherwise specified.

Preparation of RuO_2-HEAE

For the preparation of RuO_2-HEAE catalyst, 0.83 mmol of $RuCl_3 \times H_2O$, 0.055 mol of $CoCl_2 \cdot 6H_2O$, $NiCl_2 \cdot 6H_2O$, $CuCl_2 \cdot 6H_2O$, $MnCl_2 \cdot 4H_2O$, and $SmCl_3 \cdot 6H_2O$ solution (the molar ratio of Ru and HEAE (Co, Ni, Cu, Mn, Sm) is 3:1) were mixed with 1 M HCl. 0.4 g of commercial carbon (BP2000) was added and dispersed by stirring for one day at 25 °C to verify homogeneously dispersed. Then, the

mixed solution was conducted by a rotary evaporator and collected the precursor. The precursor was annealed in Ar/H_2 at 900 °C for 2 h and then annealed in air at 450 °C for 3 h. Finally, 0.1 g of powder was mixed with 0.04 L of 1 M HCl for half of the day at 25 °C, and centrifugal washing with water several times and drying to gain the final RuO_2-HEAE. Moreover, pure RuO_2 and RuO_2-TM (TM = Co, Ni, Cu, and Mn) was synthesized in a similar method using $RuCl_3 \times H_2O$ as precursor.

Structure characterization. XRD patterns of catalysts were performed on a Japan Rigaku DMax-γA rotation anode X-ray diffractometer equipped with graphite monochromatized Cu Kα radiation ($λ = 1.54178$ Å). The catalyst powder was evenly spread and compressed on a sample holder. XRD testing was conducted with a step size of 0.02°, within a range of 5–90°, with each step lasting 0.14 s, under ambient room temperature and pressure conditions. TEM images were collected on a FEI Talos F200× microscope. The catalyst powder was dispersed in ethanol, followed by taking 10 μL of ink and dropping it onto a molybdenum grid. The grid was then placed into the sample chamber. Prior to TEM testing, the vacuum was reduced to 2×10^{-5} Pa, with a humidity of 50% and a temperature of 20 °C. Aberration-corrected HADDF-STEM images and energy-dispersive X-ray spectroscopy (EDX) spectra were conducted on a JEM-ARM300F S/STEM (JEOL) operating at 300 kV. X-ray photoelectron spectroscopy

(XPS) analyses were conducted on the Thermo ESCALAB 250XI instrument utilizing an Al Kα monochromated source operating at 150 W with a photon energy of 1486.6 eV. Place a small amount of the sample on weighing paper, cut a square piece of 3 M tape, fold the weighing paper in half, place the sample on one half, use tweezers to pick up the sample to remove any excess, cover the entire 3 M tape, press gently with a tool, then pick up with tweezers and blow dry the surface of the sample with an ear syringe. Fix the 3 M tape containing the sample with double-sided tape on the sample holder, then place it in the sample chamber, evacuate to 1.8×10^{-8} Pa, at 36% humidity, and conduct XPS testing at room temperature. The concentrations of Ru, Co, Ni, Cu, Mn, and Sm were determined using an ICPE9000 instrument inductively coupled plasma mass spectrometer (ICP-MS). The catalyst underwent dispersion and dissolution in aqua regia at 25 °C before analysis by ICP-MS. Before measuring via ICP-MS, the analysis of dissolved Ru, Co, Ni, Cu, Mn, and Sm in the electrolyte involved diluting the electrolyte to 5 mL. Ru, Co, Ni, Cu, and Mn K-edge measurements were conducted at the BL14W1 beamline of Shanghai Synchrotron Radiation Facility (SSRF) and 1W1B beamline of Beijing Synchrotron Radiation Facility, China. All XAS measurements were conducted at room temperature under ambient pressure conditions. The catalyst powder was pressed with graphite in a specific ratio, encapsulated in tape, and securely positioned within the beam spot for testing. The initial XAFS data underwent processing steps such as background subtraction, normalization, and Fourier transformation following standard protocols integrated within the Athena module of the IFEFFIT software suite. The subsequent EXAFS analysis was conducted using the Artemis module, applying the specified EXAFS equation:

$$\chi(k) = \sum_j \frac{N_j S_0^2 F_j(k)}{k R_j^2} \exp[-2k^2\sigma_j^2] \exp\left[\frac{-2R_j}{\lambda(k)}\right] \sin[2kR_j + \varnothing_j(k)] \quad (1)$$

Here, S_0^2 represents the amplitude reduction factor, $F_j(k)$ denotes the effective curved-wave backscattering amplitude, N_j signifies the count of neighbors in the j_{th} atomic shell, R_j indicates the distance between the X-ray absorbing central atom and the atoms within the j_{th} atomic shell, λ reflects the mean free path in angstroms, $\phi_j(k)$ represents the phase shift, and σ_j^2 stands for the Debye-Waller parameter pertaining to the j_{th} atomic shell, showcasing the variance of distances around the mean R_j.

Operando ATR-SEIRAS. The operando Attenuated Total Reflection Surface-Enhanced Infrared Absorption Spectroscopy measurement was conducted at the BL01B infrared beamline of the Hefei Light Source utilizing a specially designed top-plate cell-reflection configuration. A ZnSe crystal was utilized as the infrared transmission window (cut-off wavenumber ≈ 625 cm^{-1}), in conjunction with an FTIR spectrometer (Bruker 70 v/s) equipped with a KBr beamsplitter and multiple detectors, including a liquid nitrogen-cooled mercury cadmium telluride detector, and integrated with an infrared microscope (Bruker Hyperion 2000 featuring a 15 × objective). During the experimental procedures, the catalyst electrode was firmly pressed against the ZnSe crystal window surface, maintaining a micron-scale gap to minimize infrared light loss. Spectral fidelity was ensured through a reflection mode with vertically incident infrared radiation. All infrared absorption spectra were obtained by averaging 128 scans at a resolution of 4 cm^{-1}. Prior to each systematic measurement, background spectra of the catalyst electrode were recorded at open-circuit potential. The potential range was set from 1.2 to 1.8 V (vs. RHE), with all electrochemical assessments conducted in a 0.1 M HClO$_4$ electrolyte. The loading amount for each measurement was consistently maintained at 40 µg (20 µL).

In suit DEMS with isotope labelling. The in-suit DEMS experiments is similar to the recently reported by the Strasser group[43]. *Operando* DEMS measurements were performed using a Linglu QAS100 differential electrochemical mass spectrometer (Linglu Instruments (Shanghai) Co., Ltd.), integrated with a high vacuum chamber (-1×10^{-8} mbar). An electrochemical cell was linked to the vacuum chamber through a cold trap cooled with dry ice, strategically positioned to prevent water vapor from entering the mass spectrometer. To facilitate gas-liquid separation, the working electrode was fabricated by depositing gold (Au) onto a 40 µm thick porous polytetrafluoroethylene (PTFE) membrane with pore dimensions of 20 nm and a porosity rate of 50%. Subsequently, the catalyst ink was drop-cast onto the Au surface, achieving an effective working area of 0.5 cm^2 and a loading density of approximately 0.2 mg cm^{-2}. In this setup, a saturated Ag/AgCl electrode functioned as the reference electrode, while a Pt served as the counter electrode. The catalysts were initially labeled with ^{18}O in 2 mL of H$_2$^{18}O-supported 0.1 M HClO$_4$ electrolyte through 9 cycles of LSV scans with a scan range from 1 V to 1.8 V vs. RHE and a scan rate of 5 mV s^{-1}. Following this, the electrodes and the cell underwent rinsing with H$_2$^{16}O to eliminate surface-adsorbed H$_2$^{18}O. Subsequently, the catalysts underwent 9 cycles of LSV in 2 mL of standard H$_2$^{16}O-supported 0.1 M HClO$_4$ electrolyte. The mass spectrometer continuously monitored the real-time generation of gaseous products with varying molecular weights during the OER.

operando **XAS characterizations.** X-ray absorption fine structure (XAFS) was conducted at the BL14W1 beamline of SSRF in the 3.5 GeV storage ring, with injection currents of 220 mA. In the measurement, a Si (111) double-crystal monochromator was used. Ru foil was used as reference samples and measured in the transmission mode. The obtained spectra were processed using Demeter software. The in situ measurement was conducted using a home-made in-situ XAFS fluorescence cell. A Pt wire and an Ag/AgCl electrode were used as the counter and reference electrodes, respectively. The working electrodes were prepared by depositing catalysts (The catalyst powders were uniformly dispersed in a mixture of isopropanol and Nafion (v:v = 19:1) to form an ink) on hydrophobic carbon paper with the content of 5 mg/ cm^2, 0.1 M HClO$_4$ solution as the electrolyte and the potentials were set as 1.2 V RHE, 1.4 V RHE, 1.6 V RHE, and OCV. During the *operando* XAFS spectral data acquisition at the Ru K-edge (22117 eV), the positions of absorption edges (E_0) were calibrated utilizing Ru foil standard samples. The collection of all spectra occurred within the same beamtime employing fluorescence mode to guarantee comparability.

Electrochemical testing. The electrocatalytic evaluation of OER activity of catalysts was carried out using a standard three-electrode cell in a 0.1 M HClO$_4$ solution. The working electrode was prepared by mixing 5 mg of catalysts with 950 µL of isopropanol and 50 µL of Nafion (5 wt%). Subsequently, 25 µL of the ink was deposited onto carbon papers (0.25 cm^2) to achieve a specific loading amount, resulting in a catalyst loading of 0.5 mg cm^{-2}. Based on the Inductively Coupled Plasma Mass Spectrometry (ICP-MS) results, the Ru content in the catalyst was determined to be approximately 30%. Consequently, the Ru content on the working electrode was estimated to be around 0.15 mg cm^{-2}. All LSV curves recorded in the three-electrode cell were iR-corrected (90%) unless specified otherwise, with the measured resistance (R) reported as 2.2 ± 0.1 Ω. For the electrolyte preparation, 4.3 mL of perchloric acid (pH = 1.1 ± 0.05) was added to a beaker containing deionized water, with the volume adjusted to 500 mL in a volumetric flask and thoroughly mixed. The reference electrode was calibrated in a three-electrode system consisting of Pt nets serving as both the working electrode and counter electrode in an H$_2$-saturated 0.1 M HClO$_4$ electrolyte. All potentials were referenced to the Reversible Hydrogen Electrode (RHE) using the equation [E (V vs. RHE) = 0.188 + 0.059 × pH]. An Ag/AgCl electrode and Pt net were employed

as the reference and counter electrodes, respectively. The stability test was conducted at 25 °C using a CHI 760E electrochemistry workstation. The LSV curves, with iR compensation correction, were obtained over the potential range from 1 to 1.8 V versus RHE at a scan rate of 5 mV s^{-1} to evaluate the OER performance of the materials. The overpotential (η) of the OER was calculated as $\eta = E_{RHE} - 1.23$ V. The Tafel slope was determined using the Tafel equation: $\eta = b \log j + a$, where b represents the Tafel slope and j is the current density. Additionally, EIS was conducted in the frequency range from 0.1 to 10^6 Hz with an amplitude of 5 mV. The electrochemical double-layer capacitances of the catalysts were acquired from cyclic voltammetry (CV) curves in the non-Faradaic range with scan rates ranging from 20 to 80 mV s^{-1}. The C_{dl} value was determined by fitting the slope of the plot of current density versus scan rate. The ECSA of the catalysts was estimated from the electrochemical double-layer capacitance (C_{dl}) of the catalytic surface using a specific equation[55].

$$ECSA = \frac{C_{dl}}{C_S}$$

The TOF is calculated from the equation below[56]:

$$TOF = \frac{J \times A}{4 \times F \times n}$$

Where J is the current density at a given overpotential, A is the surface area of the electrode, F is the Faraday constant, and n is the mole number of active metals on the electrode. The number n was estimated via the total loading mass, according to the equation:

$$n = \frac{m}{M_W}$$

where m is the loading mass, M_w is the molecular weight of the catalysts.

PEMWE evaluation

Ink preparation process. 10 mg of RuO$_2$-HEAE catalyst was dispersed in 950 μL of isopropanol and 50 μL of Nafion solution, and subjected to constant temperature ultrasonication for 1 h to obtain a uniformly dispersed anode slurry. Similarly, 10 mg of commercial Pt/C catalyst (20%, HESEN) was dispersed in 940 μL of isopropanol and 60 μL of Nafion solution, and subjected to constant temperature ultrasonication for 1 h to obtain a uniformly dispersed cathode slurry.

Membrane electrode assembly (MEA) fabrication process. The proton exchange membrane (N-115, Chemours) was cut into an area of 7.5 × 7.5 cm, and placed in an ultrasonic spray coating device (Hangzhou Chifei Ultrasonic Equipment Co., Ltd., model UAM400). A custom mask (outer frame 7.5 × 7.5 cm, exposed area in the center 1 or 5 cm^2) was overlaid on the proton exchange membrane, vacuum adsorption was initiated at a pressure of 0.3 MPa, and the temperature of the vacuum adsorption heating plate was set to 90 °C. After reaching the desired temperature, the cathode catalytic layer was sprayed. The sprayed area was 6 cm^2, completely covering the target area, at a spraying speed of 6000 mm min^{-1}, a spraying rate of 1.0 mL min^{-1}. Upon completion of spraying, X-ray fluorescence (XRF) was used to test the noble metal loading until the set target value was achieved, then spraying was stopped (Pt: 0.3 mg cm^{-2}, Ru: 0.6 mg cm^{-2}). After the cathode spraying was completed, the anode catalytic layer was sprayed by flipping the proton exchange membrane so that the cathode catalytic layer faced downwards. The anode slurry was introduced into the spraying device with the same parameters as before. After spraying, XRF (HITACHI, X-MET8000) was used to measure the noble metal loading in the anode until the target set value was reached, then spraying was stopped.

Hot pressing. After spraying, the membrane electrode was sandwiched between PTFE films and placed between two parallel stainless steel plates in a hot press machine. The assembly was subjected to hot pressing at a temperature of 130 °C and a pressure of 3 MPa for 3 min.

Device assembly. The assembled membrane electrode after hot pressing was assembled in the following order: cathode end plate, current collector plate, flow field plate, cathode diffusion layer (carbon paper, Freudenberg, E20H), membrane electrode, anode diffusion layer (Ti mesh, Bekaert, 2GDL10-0.25), flow field plate, current collector plate, anode end plate. The assembly was tightened in a star pattern with each bolt torqued to 5 N·m. The area of the flow field plate was 5 cm^2 and had been platinum-plated, with a platinum loading of 0.3 mg cm^{-2}.

Performance testing. The assembled fixture was connected to a testing power supply (NEWARE, CT-4004-5V100A), with the positive pole connected to the anode and the negative pole connected to the cathode. The test temperature was set to 80 °C with a water flow rate of 40 mL min^{-1}. After reaching the temperature, an activation process was conducted (operated under 0.1 A cm^{-2} for 30 min, then under 1 A cm^{-2} for 30 min. Finally, operated at 1.7 V for 60 min). Following activation, polarization curve testing and stability testing were carried out.

DFT calcualtions. First-principles were conducted by spin-polarized DFT[57] within projector augmented wave, which was implemented in the Vienna ab initio simulation package[58,59]. Exchange and correlation energy was assessed by the Perdew, Burke, and Ernzerhof (PBE) within the generalized gradient approximation[60,61]. The RuO$_2$ based catalysts with (110) surface[62] was selected as our slab model (144 atoms). A vacuum region of 15 Å was used in z direction to prevent interactions between periodic images. The electronic wave function was expanded using plane wave basis sets with a cutoff energy of 500 eV, employing a Monkhorst-Pack k-point grid of 2 × 2 × 1. The energy and force convergence criteria were established at 10^{-5} eV and 0.05 eV Å^{-1}, respectively. To account for van der Waals interactions, the dispersion-corrected PBE-D3 method within Grimme's scheme was implemented. We use the effective Hubbard-U (U$_{eff}$ = U − J) parameters that are optimized the structures, i.e., 2.00 (Ru), 5.50 (Co), 5.30 (Ni), 7.00 (Cu), 3.68 (Mn), and 5.00 (Sm). The demetallization energies were calculated according to $\Delta E = E_{surface} - nE_{doped-atom} + nE_{Ru-atom}$, where $E_{surface}$ and $E_{Ru-atom}$ denotes the total energies of the surface and surfaces with vacancy, $E_{dpoed-atom}$ represent the single atom energies. The reaction free energy of each proton-electron transfer step was calculated by $\Delta G = \Delta E + \Delta ZPE - T\Delta S$, in which the entropy for gas molecules have been corrected based on experimental data[63]. To avert calculate the energy of oxygen, experimental ΔG (4.92 eV), for full water splitting at standard conditions, has been used together with calculated energy of single water and hydrogen by computational hydrogen electrode[64].

Description of the fitting procedure and the approximations used. For data analysis, XANES spectra were aligned and normalized using the ATHENA module of IFEFFIT, followed by EXAFS background subtraction via the AUTOBK algorithm (Rbkg = 1.0 Å). Theoretical scattering paths were generated in FEFF9 based on our catalyst's DFT-optimized structure, and fitting was conducted over k = 3–14 Å^{-1} (Hanning window) and R = 1.0–2.0 Å (R = 1.0–3.7 Å for Ru-Ru), with constraints applied to coordination numbers, bond distances, Debye-Waller factors (σ^2 < 0.015 Å^2), and energy shifts.

The harmonic approximation was adopted given the room temperature conditions, and multiple scattering contributions were verified as negligible (<5%) through ARTEMIS refinement. Uncertainties in fitted parameters (95% confidence intervals) were derived from IFEFFIT covariance matrices. Furthermore, in the fitting of the second shell at the Ru K-edge, we approximated the transition metal as Ru for fitting

purposes. In addition, in the fitting of the RuO_2-based catalyst for Ru-Ru bond, the S_0^2 was fixed as 0.91 according to the commercial RuO_2. The R-factors obtained for all samples were consistently below 0.020, demonstrating the adequacy of the modeling, rational parameter settings, and consequently, the high-quality fitting results.

Data availability

The source data generated in this study are provided in the Source Data file. Source data are provided with this paper. Source data are provided with this paper.

References

1. Li, A. et al. Atomically dispersed hexavalent iridium oxide from MnO2 reduction for oxygen evolution catalysis. *Science* **384**, 666–670 (2024).
2. Chong, L. et al. La- and Mn-doped cobalt spinel oxygen evolution catalyst for proton exchange membrane electrolysis. *Science* **380**, 609–616 (2023).
3. Wu, Z. Y. et al. Non-iridium-based electrocatalyst for durable acidic oxygen evolution reaction in proton exchange membrane water electrolysis. *Nat. Mater.* **22**, 100–108 (2023).
4. Hao, S. et al. Torsion strained iridium oxide for efficient acidic water oxidation in proton exchange membrane electrolyzers. *Nat. Nanotechnol.* **16**, 1371–1377 (2021).
5. Xu, J. et al. $IrO_x \cdot nH_2O$ with lattice water-assisted oxygen exchange for high-performance proton exchange membrane water electrolyzers. *Sci. Adv.* **9**, eadh1718 (2023).
6. Hu, C. et al. Misoriented high-entropy iridium ruthenium oxide for acidic water splitting. *Sci. Adv.* **9**, eadf9144 (2023).
7. Lei, X. et al. High-entropy single-atom activated carbon catalysts for sustainable oxygen electrocatalysis. *Nat. Sustain.* **6**, 816–826 (2023).
8. Jin, H. et al. Dynamic rhenium dopant boosts ruthenium oxide for durable oxygen evolution. Nat. Commun. **14**, 354 (2023).
9. Abed, J. et al. Pourbaix machine learning framework identifies acidic water oxidation catalysts exhibiting suppressed ruthenium dissolution. *J. Am. Chem. Soc.* **146**, 15740–15740 (2024).
10. Han, N. et al. Lowering the kinetic barrier via enhancing electrophilicity of surface oxygen to boost acidic oxygen evolution reaction. *Matter* **7**, 1–14 (2024).
11. Li, S. et al. Highly efficient anion exchange membrane water electrolyzers via chromium-doped amorphous electrocatalysts. *Nat. Commun.* **15**, 3416 (2024).
12. Rao, R. R. et al. Operando identification of site-dependent water oxidation activity on ruthenium dioxide single-crystal surfaces. *Nat. Catal.* **3**, 516–525 (2020).
13. Wang, J. et al. Single-site Pt-doped RuO_2 hollow nanospheres with interstitial C for high-performance acidic overall water splitting. *Sci. Adv.* **8**, eabl9271 (2022).
14. Yao, Y. et al. Engineering the electronic structure of single atom Ru sites via compressive strain boosts acidic water oxidation electrocatalysis. *Nat. Catal.* **2**, 304–313 (2019).
15. Wang, Y. et al. Unraveling oxygen vacancy site mechanism of Rh-doped RuO_2 catalyst for long-lasting acidic water oxidation. *Nat. Commun.* **14**, 1412–1422 (2023).
16. Shi, Z. et al. Customized reaction route for ruthenium oxide towards stabilized water oxidation in high-performance PEM electrolyzers. *Nat. Commun.* **14**, 843 (2023).
17. Li, L. et al. Lanthanide-regulating Ru-O covalency optimizes acidic oxygen evolution electrocatalysis. *Nat. Commun.* **15**, 4974–4982 (2024).
18. Zuo, S. et al. Local compressive strain-induced anti-corrosion over isolated Ru-decorated Co_3O_4 for efficient acidic oxygen evolution. *Nat. Commun.* **15**, https://doi.org/10.1038/s41467-024-53763-8 (2024).
19. Chen, F.-Y., Wu, Z.-Y., Adler, Z. & Wang, H. Stability challenges of electrocatalytic oxygen evolution reaction: From mechanistic understanding to reactor design. *Joule* **5**, 1704–1731 (2021).
20. Tiwari, J. N. et al. Multi-heteroatom-doped carbon from waste-yeast biomass for sustained water splitting. *Nat. Sustain.* **3**, 556–563 (2020).
21. Hao, Y. et al. Polarized ultrathin BN induced dynamic electron interactions for enhancing acidic oxygen evolution. *Angew. Chem. Int. Ed.* **63**, e202402018 (2024).
22. Yao, N. et al. Atomically dispersed Ru oxide catalyst with lattice oxygen participation for efficient acidic water oxidation. *Chem* **9**, 1882–1896 (2023).
23. Sun, P. et al. Designing 3d transition metal cation-doped $MRuO_x$ as durable acidic oxygen evolution electrocatalysts for PEM water electrolyzers. *J. Am. Chem. Soc.* **146**, 15515–15524 (2024).
24. Chang, J. et al. Oxygen radical coupling on short-range ordered Ru atom arrays enables exceptional activity and stability for acidic water oxidation. *J. Am. Chem. Soc.* **146**, 12958–12968 (2024).
25. Zu, L. et al. Self-assembly of Ir-based nanosheets with ordered interlayer space for enhanced electrocatalytic water oxidation. *J. Am. Chem. Soc.* **144**, 2208–2217 (2022).
26. Gayen, P., Saha, S., Liu, X., Sharma, K. & Ramani, V. K. High-performance AEM unitized regenerative fuel cell using Pt-pyrochlore as bifunctional oxygen electrocatalyst. *Proc. Natl. Acad. Sci.* **118**, e2107205118 (2021).
27. Du, K. et al. Interface engineering breaks both stability and activity limits of RuO_2 for sustainable water oxidation. *Nat. Commun.* **13**, 5448 (2022).
28. Grimaud, A. et al. Activating lattice oxygen redox reactions in metal oxides to catalyse oxygen evolution. *Nat. Chem.* **9**, 457–465 (2017).
29. Wang, X. et al. Pivotal role of reversible NiO_6 geometric conversion in oxygen evolution. *Nature* **611**, 702–708 (2022).
30. Lin, C. et al. In-situ reconstructed Ru atom array on α-MnO_2 with enhanced performance for acidic water oxidation. *Nat. Catal.* **4**, 1012–1023 (2021).
31. Zhang, D. et al. Construction of Zn-doped RuO_2 nanowires for efficient and stable water oxidation in acidic media. *Nat. Commun.* **14**, 2517 (2023).
32. Zhou, W. et al. Regulating the scaling relationship for high catalytic kinetics and selectivity of the oxygen reduction reaction. *Nat. Commun.* **13**, 6414–6424 (2022).
33. Zhu, H. et al. A high-entropy atomic environment converts inactive to active sites for electrocatalysis. *Energ. Environ. Sci.* **16**, 619–628 (2023).
34. Yang, C.-L. et al. Sulfur-anchoring synthesis of platinum intermetallic nanoparticle catalysts for fuel cells. *Science* **374**, 459–464 (2021).
35. Ping, X. et al. Locking the lattice oxygen in RuO_2 to stabilize highly active Ru sites in acidic water oxidation. *Nat. Commun.* **15**, 2501–2511 (2024).
36. Wang, J. et al. Exceptionally active and stable RuO_2 with interstitial carbon for water oxidation in acid. *Chem* **8**, 1673–1687 (2022).
37. McKeown, D. A. et al. Structure of hydrous ruthenium oxides: implications for charge storage. *J. Phys. Chem. B* **103**, 4825–4832 (1999).
38. Zhao, Z. L. et al. Boosting the oxygen evolution reaction using defect-rich ultra-thin ruthenium oxide nanosheets in acidic media. *Energ. Environ. Sci.* **13**, 5143–5151 (2020).
39. Cheng, W., Su, H. & Liu, Q. Tracking the oxygen dynamics of solid-liquid electrochemical interfaces by correlative in situ synchrotron spectroscopies. *Acc. Chem. Res.* **55**, 1949–1959 (2022).
40. Su, H. et al. Dynamic evolution of solid-liquid electrochemical interfaces over single-atom active sites. *J. Am. Chem. Soc.* **142**, 12306–12313 (2020).

41. Su, H. et al. Tensile straining of iridium sites in manganese oxides for proton-exchange membrane water electrolysers. *Nat. Commun.* **15**, 95–106 (2024).

42. Fan, R. et al. Ultrastable electrocatalytic seawater splitting at ampere-level current density. *Nat. Sustain.* **7**, 158–167 (2024).

43. Görlin, M. et al. Oxygen evolution reaction dynamics, faradaic charge efficiency, and the active metal redox states of Ni–Fe oxide water splitting electrocatalysts. *J. Am. Chem. Soc.* **138**, 5603–5614 (2016).

44. Scott, S. B. et al. The low overpotential regime of acidic water oxidation Part II: trends in metal and oxygen stability numbers. *Energy Environ. Sci.* **15**, 1988–2001 (2022).

45. Kasian, O. et al. Degradation of iridium oxides via oxygen evolution from the lattice: correlating atomic scale structure with reaction mechanisms. *Energ. Environ. Sci.* **12**, 3548–3555 (2019).

46. Zhou, Y. et al. Asymmetric dinitrogen-coordinated nickel single-atomic sites for efficient CO_2 electroreduction. *Nat. Commun.* **14**, 3776–3786 (2023).

47. Lang, C. et al. Observation of a potential-dependent switch of water-oxidation mechanism on Co-oxide-based catalysts. *Chem* **7**, 2101–2117 (2021).

48. Wang, B. et al. In situ structural evolution of the multi-site alloy electrocatalyst to manipulate the intermediate for enhanced water oxidation reaction. *Energ. Environ. Sci.* **13**, 2200–2208 (2020).

49. de Almeida, J. S. & Ahuja, R. Electronic and optical properties of RuO_2 and IrO_2. *Phys. Rev. B* **73**, 165102 (2006).

50. Liang, Q., Bieberle-Hütter, A. & Brocks, G. Anti-ferromagnetic RuO_2: a stable and robust OER catalyst over a large range of surface terminations. *J. Phys. Chem. C.* **126**, 1337–1345 (2022).

51. Mehtougui, N. et al. Structural, electronic and mechanical properties of RuO_2 from first-principles calculations. *Mat. Sci. Semicon. Proc.* **15**, 331–339 (2012).

52. Vonrüti, N., Rao, R., Giordano, L., Shao-Horn, Y. & Aschauer, U. Implications of nonelectrochemical reaction steps on the oxygen evolution reaction: oxygen dimer formation on perovskite oxide and oxynitride surfaces. *ACS Catal.* **12**, 1433–1442 (2022).

53. Reier, T., Nong, H. N., Teschner, D., Schlögl, R. & Strasser, P. Electrocatalytic oxygen evolution reaction in acidic environments-reaction mechanisms and catalysts. *Adv. Energy Mater.* **7**, 1601275–1601293 (2016).

54. Dickens, C. F. & Nørskov, J. K. A theoretical investigation into the role of surface defects for oxygen evolution on RuO_2. *J. Phys. Chem. C.* **121**, 18516–18524 (2017).

55. He, X. et al. Hexafluorophosphate additive enables durable seawater oxidation at ampere-level current density. *Nat. Commun.* **16**, https://doi.org/10.1038/s41467-025-60413-0 (2025).

56. Gao, R. & Yan, D. Fast formation of single-unit-cell-thick and defect-rich layered double hydroxide nanosheets with highly enhanced oxygen evolution reaction for water splitting. *Nano Res.* **11**, 1883–1894 (2018).

57. Hohenberg, P. & Kohn, W. Inhomogeneous electron gas. *Phys. Rev.* **136**, B864–B871 (1964).

58. Blöchl, P. E., Jepsen, O. & Andersen, O. K. Improved tetrahedron method for Brillouin-zone integrations. *Phys. Rev. B* **49**, 16223–16233 (1994).

59. Kresse, G. & Furthmuller, J. Efficient iterative schemes for ab initio total-energy calculations using a plane-wave basis set. *Phys. Rev. B* **54**, 11169–11186 (1996).

60. Kohn, W. & Sham, L. J. Self-consistent equations including exchange and correlation effects. *Phys. Rev.* **140**, A1133–A1138 (1965).

61. Kresse, G. & Joubert, D. From ultrasoft pseudopotentials to the projector augmented-wave method. *Phys. Rev. B* **59**, 1758–1774 (1999).

62. Fang, Y.-H. & Liu, Z.-P. Mechanism and Tafel lines of electro-oxidation of water to oxygen on RuO2(110). *J. Am. Chem. Soc.* **132**, 18214–18222 (2010).

63. Liang, W., Chen, J., Liu, Y. & Chen, S. Density-functional-theory calculation analysis of active sites for four-electron reduction of O_2 on Fe/N-doped graphene. *ACS Catal.* **4**, 4170–4177 (2014).

64. Rossmeisl, J., Logadottir, A. & Nørskov, J. K. Electrolysis of water on (oxidized) metal surfaces. *Chem. Phys.* **319**, 178–184 (2005).

Acknowledgements

Author contributions

S.C., Q.C., and L.S. conceived the project design. F.Q., L.Y., J.H., and C.H. prepared the samples and measured their electrochemical properties. F.Q., D.C., S.C., W.J., B.S., and L.S. performed the XAS and TEM characterizations. F.Q., Y.Y., K.C., and Z.W. analyzed the proton exchange membrane (PEM) electrolyzer. F.Q., D.C., and H.L. performed the operando measurements and analyzed the data. F.Q. and X.W. performed the DFT calculations. F.Q. and H.L. drew the figures. F.Q., S.C., P.C., Q.C., and L.S. wrote and revised the paper with help from all authors.

Competing interests

The authors declare no competing interests.

Additional information